

On the X-ray Baldwin effect for narrow Fe K α emission line

P. Jiang, J. X. Wang, and T. G. Wang

*Center for Astrophysics, University of Science and Technology of China, Hefei, Anhui
230026, P. R. China*

Joint Institute of Galaxies and Cosmology, USTC and SHAO, CAS

jpaty@mail.ustc.edu.cn

ABSTRACT

Most Active Galactic Nuclei (AGN) exhibit a narrow Fe K α line at ~ 6.4 keV in the X-ray spectra, due to the fluorescent emission from cold material far from the inner accretion disk. Using *XMM-Newton* observations, Page et al. found that the equivalent width (EW) of the narrow Fe K α line decreases with increasing luminosity ($EW \propto L^{-0.17 \pm 0.08}$), suggesting a decrease in the covering factor of the material emitting the line (presumably the torus). By combining the archival *Chandra* HETG observations of 34 type 1 AGNs with *XMM* observations in literature, we build a much large sample with 101 AGNs. We find a similar X-ray Baldwin effect in the sample ($EW \propto L^{-0.2015 \pm 0.0426}$), however, we note that the anti-correlation is dominated by the radio loud AGN in the sample, whose X-ray spectra might be contaminated by the relativistic jet. Excluding the radio loud AGN, we find a much weaker anti-correlation ($EW \propto L^{-0.1019 \pm 0.0524}$). We present Monte-Carlo simulations showing that such a weak anti-correlation can be attributed to the relative short time scale variations of the X-ray continuum.

Subject headings: galaxies: active – X-rays: galaxies – quasars: emission lines

1. Introduction

The iron K α emission line at ~ 6.4 keV was first identified as a common feature in the X-ray spectrum of active galactic nuclei (AGN) by *Ginga* (Pounds et al. 1990; Nandra & Pounds 1994). Its origin can be promptly interpreted as fluorescence emission following photoelectric absorption of the hard X-ray continuum (see Reynolds & Nowak 2003 for a review). In 1995, *ASCA* observation of MCG–6-30-15 yielded a broadened and skewed iron K α line profile (Tanaka et al. 1995). The line profile was successfully interpreted as fluorescence line from the innermost region of an accretion disk around a supermassive black

hole. This is the first direct evidence of emission from an accretion disk extending down to a few Schwarzschild radii. Thereafter, the iron $K\alpha$ emission line became one of the major targets of X-ray astronomy studies.

Recent *XMM-Newton* and *Chandra* observations revealed narrow (unresolved by *XMM*) iron $K\alpha$ lines at $\sim 6.4\text{keV}$ in the X-ray spectra of most AGNs (e.g. Yaqoob & Padmanabhan 2004; Page et al. 2004a). Contrary to previous low-resolution *ASCA* observations, broad iron emission lines appear to be much rarer in *XMM-Newton* and *Chandra* spectra. Different from the broad line profile, which comes from the innermost region of the accretion disk, the narrow iron $K\alpha$ is believed to be due to emission from neutral iron far from the inner accretion disk. Possible origins of the narrow line include the outermost regions of the accretion disk, the Broad Line Region, and the putative molecular torus.

In 1993, an X-ray Baldwin effect in the iron K lines was found in *Ginga* observations of 37 AGN (Iwasawa & Taniguchi 1993). They found the equivalent width (EW) of the iron K line is anti-correlated to the X-ray continuum luminosity ($\text{EW} \sim L_{2-10\text{keV}}^{-0.20 \pm 0.03}$). The trend was confirmed by later *ASCA* observations of broad iron lines (Nandra et al. 1997). Such an effect can be explained due to the presence of an ionized skin on the accretion disk, with the degree of ionization increasing with luminosity (see Nayakshin 2000a, b).

An X-ray Baldwin effect was also reported for the narrow iron $K\alpha$ line observed by *XMM-Newton* (Page et al. 2004a; Zhou & Wang 2005). Since the narrow line is produced much far away from the inner X-ray continuum source, such an effect can not be due to the change of the ionization state of the line emitting clouds. A possible explanation is a decrease in the covering factor of the material forming the fluorescence line (such as the torus) with increasing X-ray luminosity. If true, such a result supports the scheme that the lack of a large population of obscured quasars (luminous AGNs) now discovered is due to the smaller covering factor of the torus in quasars (for example, the receding torus model, see Simpson 2005). However, the X-ray Baldwin effect of the narrow iron $K\alpha$ line was questioned by *XMM-Newton* observations of PG quasars. Jiménez-Bailón et al. (2005) found the narrow iron $K\alpha$ lines in PG quasars are similar to those of Seyfert galaxies, and no X-ray Baldwin effect was found. We also note that while some studies show that the fraction of obscured AGN significantly decreases with luminosity (e.g., Ueda et al. 2003; Steffen et al. 2003), some other studies yield contrary results supporting the existence of a large population of obscured quasars (e.g. Martínez-Sansigre et al. 2005; Tozzi et al. 2005). Note a most recent work (Markwardt et al. 2005) studied the population of obscured AGN in Swift/BAT all sky survey and found a significant reduction in the fraction of absorbed/obscured AGN at higher luminosities.

In this paper we revisit this issue by studying archival AGN spectra obtained by *Chan-*

Chandra High Energy Transmission Grating Spectrometer (HETGS), which has better spectral resolution in the iron line band for more accurate measurement of the narrow Fe K line. We also combined our *Chandra* sample with *XMM* observations in literature to build a much larger sample of 75 radio quiet and 26 radio loud AGNs. We found that the previous reported X-ray Baldwin effect is mainly due to the radio loud sources in their sample, whose X-ray spectra might be contaminated by the relativistic jet. We found a much weaker X-ray Baldwin effect of the narrow iron K α line for radio quiet sample, however, we present simulations showing that such a weak anti-correlation is indistinguishable from an observational bias due to the variation of AGN X-ray continuum. Throughout this paper, H_0 is taken to be $70 \text{ km s}^{-1} \text{ Mpc}^{-1}$, $\Omega_m=0.27$ and $\Omega_\lambda=0.73$.

2. Chandra observations and data analysis

We searched for archival *Chandra* HETGS observations as of 2005 September 20 in the *Chandra* archive database¹. The search revealed 89 HETGS observations of 44 type 1 Seyfert galaxies and QSOs. Type 2 sources were excluded because for most of them it is difficult to measure the intrinsic X-ray luminosities due to strong absorption. HETGS consists of two grating assemblies, a High Energy Grating (HEG) and a Medium Energy Grating (MEG). Our study will focus on the HEG data, which have better spectral resolution and larger effective area in the Fe K α band. We also excluded 8 observations: MKN421 (Obsid 457), PG 1404+226 (812), 1H 070-495 (862 and 2304), MCG-5-23-16 (2121-1e and 2121-2e), 1H 0414+009 (2969), MRK 705 (4914), whose HEG count rates are too low for spectral fitting, and 3 high redshift QSOs (Q 0836+7104, PKS 2149-306, PKS 1830-211) because the center of their Fe K α lines in the observed frame were out of our restricted band (mentioned below). Finally, we obtained 74 observations of 34 Seyfert 1 galaxies and QSOs from *Chandra*.

We used the first order of the HEG grating data by combining the positive and negative arms. For the sources with multiple observations, we used the observation with the longest exposure time. We used XSPEC version 11.3.2l (Arnaud 1996) for spectral fitting. To utilizing the highest possible spectral resolution available, we binned the spectra to the intrinsic resolution of the HEG (one bin is 0.012\AA), and adopt the *C*-statistic (Cash 1976) for minimization. Our model is a power-law plus a Gaussian emission line with possible intrinsic neutral absorption. The Galactic absorption was also accounted. We restrict our fit to 2.5 – 8. keV band to avoid possible complex absorption and/or soft excess at lower energy. During the fit, the background was subtracted.

¹See <http://cda.harvard.edu/chaser>

For PDS 456, ARK 564, 3C 273, PKS 2155-304, NGC 3227, MKN 421, an Fe K emission line was not detected. We obtained the upper limits on the equivalent width (EW) for such sources by fixing the line width to 1000 km s^{-1} and the rest frame line energy at 6.4 keV. For MKN 766, 3C 379, 4c 74.56, 1 ES 1028+511, IC 4329a, NGC 526a, NGC 985 and EOS 198-G24 the narrow emission line was not resolved, we thus gave constraints on the line energy and EW by fixing the line width to 1000 km s^{-1} . For NGC 7314 and H 1821+643 obvious broad Fe K line can be detected with $\text{FWHM} \geq 10000 \text{ km s}^{-1}$, for which we also fixed the line width at 1000 km s^{-1} to measure the line flux of the narrow core. For MCG-6-30-15 whose Fe K line profile is very complex, we used the luminosity and narrow line equivalent width obtained by Yaqoob & Padmanabhan (2004) directly. And for other unresolved objects (MKN 590, MRC 2251-178, H 1821+643 and H 1426+428) XSPEC could not give the best line energy while fixing the line width, so we also fixed the line energy. For other sources, all three parameters of the Gaussian line were set free during the fit. (See Table 1).

3. Statistical analysis

The Astronomy Survival Analysis (ASURV; Feigelson & Nelson, 1985) Package can be used in the presence of censored (upper limit) data. This allows us to study the relationship between line EW and $L_{2-10\text{keV}}$, including all significant and non-significant detections of the narrow lines. We performed the Spearman Rank (SR) statistic to give the correlation between EW and luminosity in log-log space, and performed the Buckley-James method to find the slope of the best-fit line. Figure 1a plots the rest frame EW of the narrow Fe K α line against the rest frame 2. – 10. keV luminosity for *Chandra* sources. It can be seen that the EW decreases with the increasing luminosity. The fit gives a power law index of $\alpha = -0.1940 \pm 0.0332$ (spearman's coefficient $R_s = -0.651$), where $EW \propto L^\alpha$. The result is consistent with $\alpha = -0.18 \pm 0.04$ obtained by Page et al. (2004a). For our *XMM-Newton* observations² (See Table 2), the fit gives a similar index of $\alpha = -0.2097 \pm 0.0503$ ($R_s = -0.463$) for the whole sample. However, when only the radio-quiet objects of the sample are considered (Figure 2b), the inverse correlation between EW and the luminosity becomes weaker ($\alpha = -0.1023 \pm 0.0558$, $R_s = -0.280$).

To better study the possible correlation, we combined our *Chandra* sample with our *XMM-Newton* sample to build a much larger sample with 75 radio quiet sources and 26 radio loud sources. There are 22 objects (NGC 4151, NGC 5506, NGC 3516, NGC 4593, IC

²all of them were obtained from: Page et al. (2004a), Zhou & Wang (2005), Jiménez-Bailón et al. (2005), Page et al. (2004b)

4329a, MRK 509, F9, MRC 2251-178, PDS 456, NGC 3227, MCG-6-30-15, 3C 273, MKN 766, 3C 120, akn 564, NGC 4051, NGC 7314, Mrk 279, NGC 3783, ESO 198-G24, NGC 7469 and NGC 5548) included in both our *Chandra* and *XMM-Newton* samples. Figure 3a plots their *Chandra* X-ray luminosities against *XMM* ones. Clearly, there is no systematic bias between the observed luminosities by different instruments, however, 8 out of 22 sources show variation with amplitude above 1.5. The relationship of line EW observed by *Chandra* and *XMM* is plotted in Figure 3b. We can see that most of EW observed by *Chandra* are consistent with those observed by *XMM*. Considering that *Chandra* data has better spectral resolution in the Fe K α band, which is essential to measure the narrow line, we directly adopt *Chandra* data for these 22 sources and drop *XMM* ones in the combined sample. Figure 4 plots the correlation between the EW and luminosity for all objects in the large sample ($\alpha = -0.2015 \pm 0.0426$, $R_s = -0.469$) and for radio-quiet objects only ($\alpha = -0.1019 \pm 0.0524$, $R_s = -0.266$). The fitting results are consistent with those derived from *Chandra* and *XMM* data respectively. The values for three different samples are listed together in Table 3. Note for the *Chandra* only sample, the difference between the correlation index from RQ+RL sources and RQ sources only is not obvious as for *XMM* and combined samples. This is mainly because that there is very limited number of luminous sources in the *Chandra* only sample: only one RQ sources (H 1821+643) shows L_X above $10^{45.5}$ erg s $^{-1}$, thus the correlation index is extremely sensitive to its EW measurement: for H 1821+643 we fixed the line width at 1000 km s $^{-1}$ to get an EW of 40 eV; while the best fit value gives a line width of 10000 km s $^{-1}$ and an EW of 140 eV; adopting the later values we get a linear correlation index of -0.1062 ± 0.0573 .

We can clearly see that when the RL sources were excluded from the sample the correlation between the line EW and X-ray luminosity became much weaker (with a confidence level less than 2σ). To show the results more clearly, in Figure 5 we plot the mean EW for 5 luminosity bins for all AGNs and just the radio-quiet objects in the combined sample. Following Page et al. (2004a), the upper limits were taken to be half of the value, together with an equally sized error bar. Similar to Page et al., we find a clear anti-correlation for RQ+RL sources (Figure 5a). However, for RQ only sources, we see no anti-correlation in Figure 5b.

4. Time variation model

Suggestions for the origin of the neutral Fe K α line include the putative molecular torus and/or the BLR (broad-line region). Since produced at a much larger scale, the line should exhibit no significant fluctuations within a timescale of months to years, while the behavior

of the X-ray continuum is much more active within much shorter timescales (Krolik et al. 1993). As a result, the observed equivalent width of the narrow line would be surely smaller while the X-ray continuum is in a higher state, and vice versa. For instance, Figure 6 plots the observations of NGC 3783 and NGC 4151 with *Chandra* (the only two radio quiet sources with more than two *Chandra* HETG observations) and the best-fit lines. Although there are only 6 points for NGC 3783 and 3 points for NGC 4151, we performed a linear regression to give the best-fit slopes of them ($\alpha = -1.7752 \pm 0.8130$, $R_s = -0.657$ for NGC 3783 and $\alpha = -1.5244 \pm 0.0732$, $R_s = -1.000$ for NGC 4151). As expected, its EW clearly decreases with increasing luminosity. Such an effect may naturally lead to the observed anti-correlation slope between the EW and luminosity for a sample of AGN. In this section we run Monte-Carlo simulations to check this possibility.

An anti-correlation between the X-ray luminosity and long term variation amplitude in Seyfert 1 galaxies was described by Markovitz & Edelson (2004). Fractional variability amplitudes (F_{var}) were measured for each light curve to quantify the intrinsic variability amplitude.

$$F_{var} = \sqrt{\frac{S^2 - \langle \sigma_{err}^2 \rangle}{\langle X \rangle^2}}$$

where S^2 is the total variance of the light curve, $\langle \sigma_{err}^2 \rangle$ is the mean error squared and $\langle X \rangle$ is the mean count rate of N total points. They gave the anti-correlation between Fractional variability amplitude and luminosity: $F_{var} \propto L_x^{-0.135}$ for long (1296 days) timescale data.

Here we adopt a toy model to simulate the X-ray continuum variation, while line flux is assumed to be invariable. The observed X-ray luminosity is assumed to be normally distributed with the width of the Gaussian distribution calculated to match the observed excess variance at different luminosities (Markovitz & Edelson 2004). By normalizing the observed line EW for the combined RQ sample (with upper limits) to the best-fit line, we first construct a set of line EW which does not correlate with the X-ray luminosity. Random continuum variations are then added to the luminosities, and the line EW are modified correspondingly since we assume no change to the line flux. We repeated this step to build 1000 artificial samples with different random seed for each time. We used ASURV to perform linear regression to the artificial samples. The distribution of the best-fit power-law slopes of the artificial samples was presented in Figure 7. We can see that 8.4% of the simulations produce anti-correlation slopes steeper than the observed value, and the mean value is -0.0485 ± 0.0536 , which is compatible with the observed value ($\alpha = -0.1019 \pm 0.0524$) within the errors.

5. CONCLUSION

In this paper, we studied the narrow iron $K\alpha$ line in 123 Seyfert 1 galaxies and QSOs with archive *Chandra* HETGS observations and *XMM* observations in literature. There is an anti-correlation between the EW of the narrow, neutral iron line observed and the X-ray continuum luminosity: as the 2-10 keV rest frame luminosity increases, the equivalent width of the line drops. One possible reason for this negative correlation is a decline in the covering factor of the putative molecular torus as the luminosity increases (Page et al. 2004a). However, because of the dilution effect of relativistic beaming in the radio loud sources, they should be excluded from the study. Although Page et al. also reported an X-ray Baldwin effect after excluding RL AGN from their sample, the effect appears to be much weaker for RQ AGN in our larger sample. We find that the observed weak anti-correlation can be explained by the observational bias cause by variable AGN X-ray continuum.

This work was supported by Chinese NSF through NSF10473009/NSF10533050 and the CAS "Bai Ren" project at University of Science and Technology of China.

REFERENCES

- Arnaud, K. A. 1996, in ASP Conf. Ser. 101, Astronomical Data Analysis software and Systems V, ed. G. Jacoby & J. Barnes (San Francisco: ASP), 17
- Cash, W. 1979, ApJ, 228, 939
- Feigelson, E. D., & Nelson, P. I. 1985, ApJ, 293, 192
- Iwasawa, K., & Taniguchi, Y. 1993, ApJ413, L15
- Jiménez-Bailón, E., Piconcelli, E., Guainazzi, M., Schartel, N., Rodríguez-Pascual, P.M., and Santos-Lleó, M. 2005, A&A, 435, 449J
- Krolik, J.H., Done, C., and Madejski, G.M. 1993, ApJ, 402, 432
- Markowitz, A., & Edelson, R. 2004, ApJ, 617, 939
- Markwardt, C. B., Tueller, J., Skinner, G. K., Gehrels, N., Barthelmy, S. D., & Mushotzky, R. F. 2005, ApJ, 633, L77
- Martínez-Sansigre, A. et al. 2005, Nature, 436, 666
- Nandra, K., & Pounds, K.A. 1994, MNRAS, 268, 558
- Nandra, K., George, I.M. Mushotzky, R.F., Turner, T.J., and Yaqoob, T. 1997, ApJ, 488,L91
- Nayakshin, S. 2000a, ApJ, 534, 718

- Nayakshin, S. 2000b, *ApJ*, 540, L37
- Page, K.L., O’Brien, P.T., Reeves, J.N., and Turner, M.J.L. 2004a, *MNRAS*, 347, 316
- Page, K.L., Reeves, J.N., O’Brien, P.T., Turner, M.J.L., and Worrall, D.M. 2004b, *MNRAS*, 353, 133
- Pounds, K.A. et al. 1990, *Nature*, 344, 132
- Reynolds, C. S., & Nowak, M. A. 2003, *Phys. Repl.*, 377, 389
- Simpson, C. 2005, *MNRAS*, 360, 565
- Steffen, A. T., Barger, A. J., Cowie, L. L., Mushotzky, R. F., & Yang, Y. 2003, *ApJ*, 596, L23
- Tanaka, Y. et al. 1995, *Nature*, 375, 659
- Tozzi, P. et al. 2006, *A&A* in press
- Ueda, Y., Akiyama, M., Ohta, K., & Miyaji, T. 2003, *ApJ*, 598, 886
- Veron-Cetty, M. P., & Veron, P. 2003, *VizieR Online Data Catalog*, 7235, 0
- Yaqoob, T., & Padmanabhan, U. 2004, *ApJ*, 604, 63Y
- Zhou, X., & Wang, J. 2005, *ApJ*, 618, L83

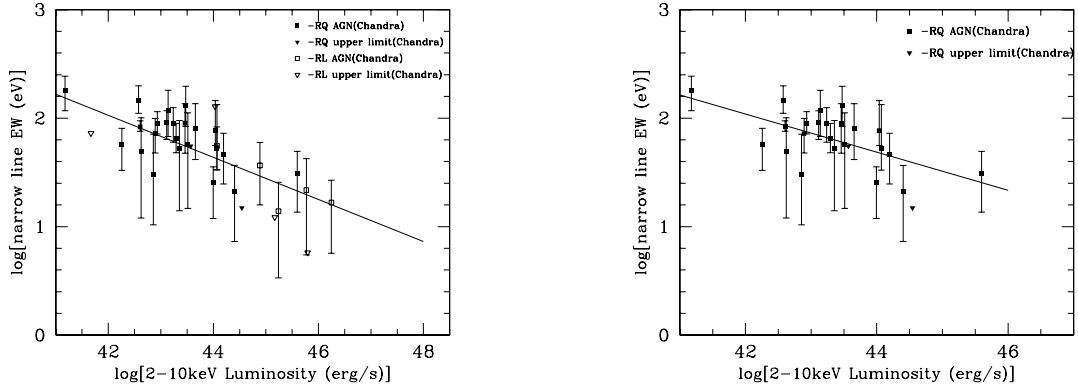


Fig. 1.— The correlation between narrow FeK line EW and luminosity for the sample of 34 Seyfert 1 galaxies and QSOs observed by *Chandra*, Left: including both radio loud objects and radio quiet objects; Right: including radio quiet objects only. The solid lines show the best-fit anti-correlation slopes.

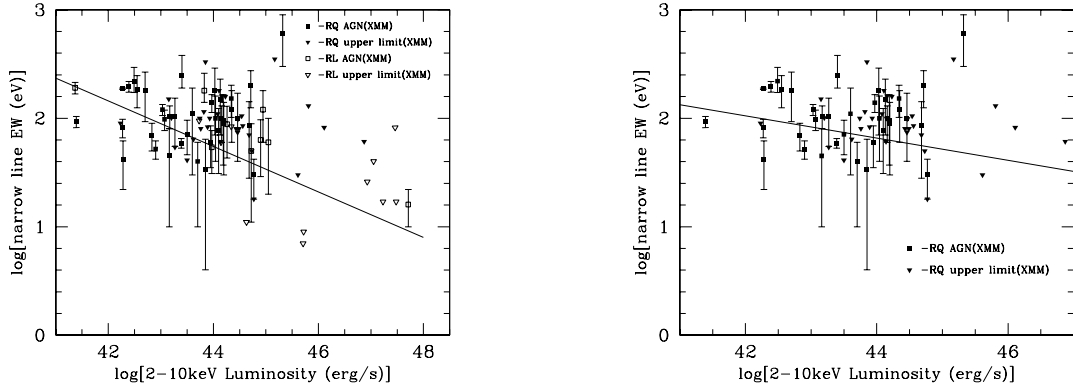


Fig. 2.— The correlation between narrow FeK line EW and luminosity for the *XMM-Newton* sample Left: including both radio loud objects and radio quiet objects; Right: including radio quiet objects only. The solid lines show the best-fit anti-correlation slopes.

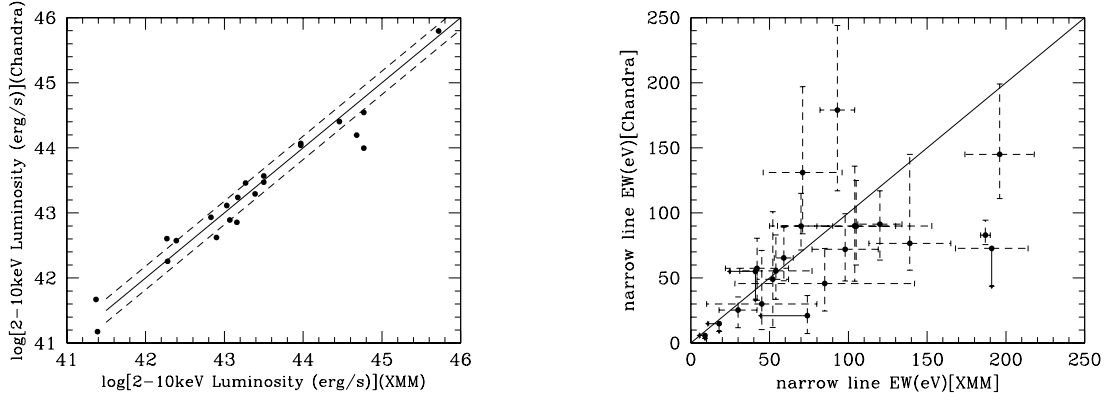


Fig. 3.— Left: The luminosities obtained by *XMM-Newton* and *Chandra* for the 22 objects observed by both observatories. Solid line indicates $\log[L_{XMM}] = \log[L_{Chandra}]$; dash lines indicate a variation amplitude of 1.5; Right: The EW observed by *XMM-Newton* and *Chandra* for the 22 objects. Solid line indicates $EW_{XMM} = EW_{Chandra}$.

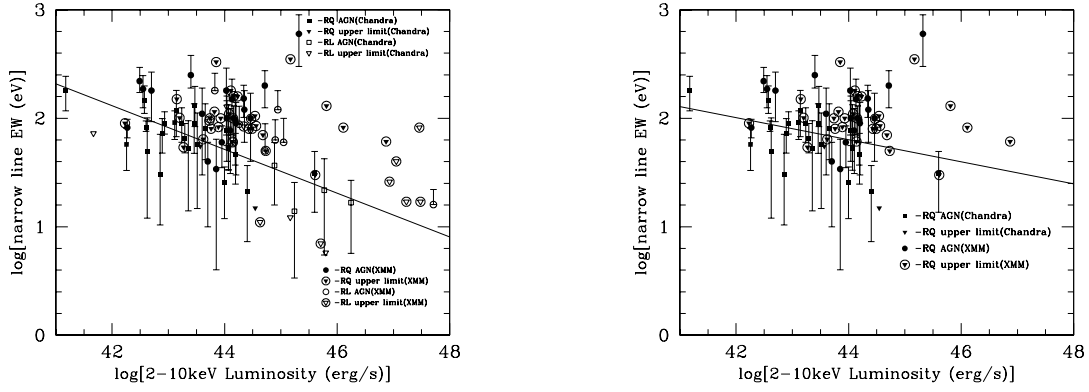


Fig. 4.— The correlation between the luminosity and the EW for the combined sample. Left: including both radio quiet sources and radio loud sources; Right: including radio quiet sources only. The solid lines show the best-fit anti-correlation slopes.

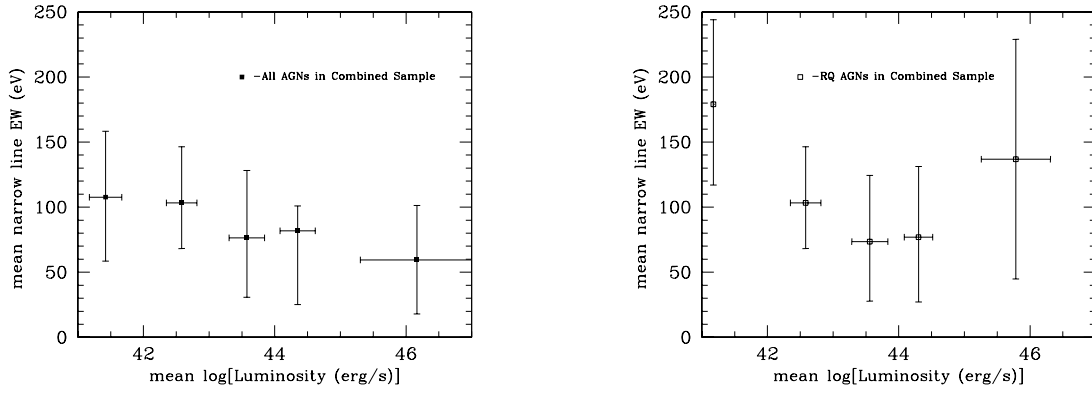


Fig. 5.— Averaging the narrow line equivalent widths within 5 luminosity bins for combined sample. Left: All AGNs in combined sample; Right: Only RQ AGNs in combined sample.

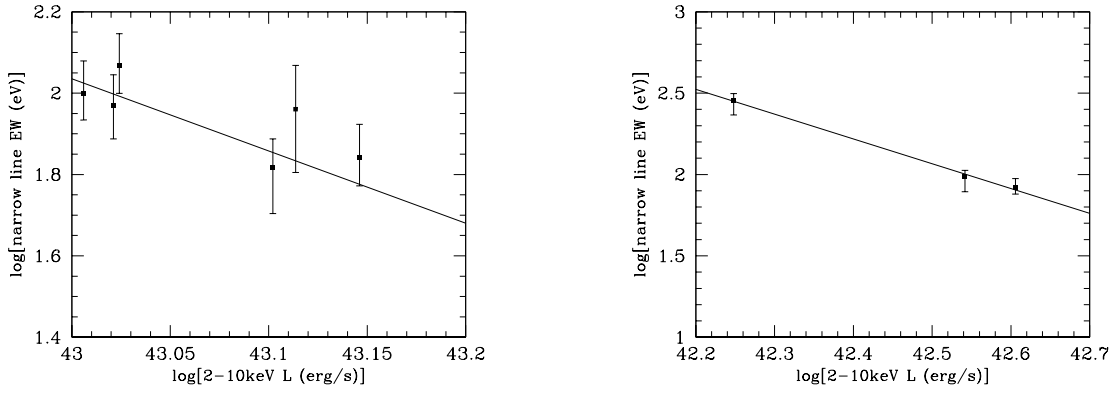


Fig. 6.— Left: Six *Chandra* HETG observations of source NGC 3783. Right: Three *Chandra* HETG observations of source NGC 4151. The solid lines show the best-fit anti-correlation slopes. See text for details.

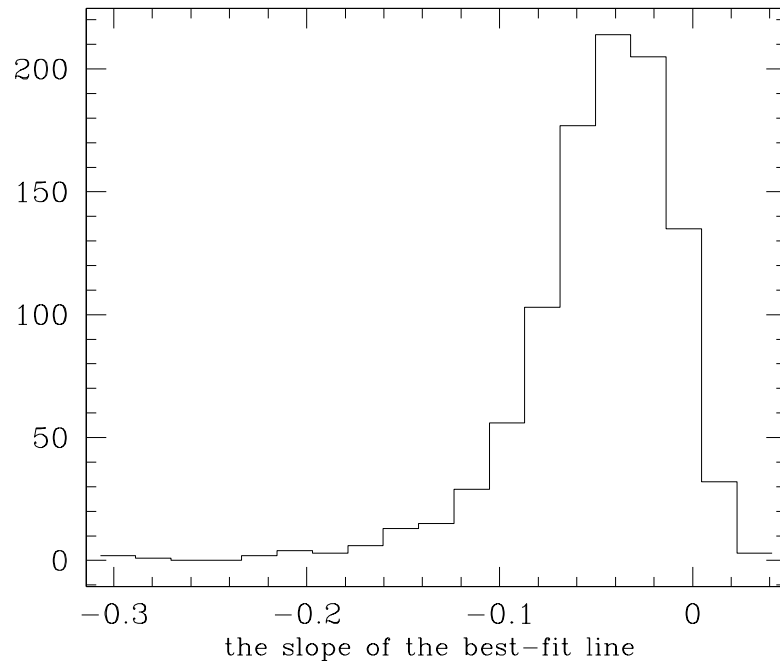


Fig. 7.— The distribution of the best-fit power-law slopes of the artificial samples.

Table 1. Parameters of the Narrow Fe K α Emission Line from *Chandra* (HEG) Data

Source	Z^a	Spectral Type	Pho.Index	$N_{H(Gal)}^b$ (10^{22} cm^{-2})	N_H^c (10^{22} cm^{-2})	E^d (keV)	$FWHM^e$ (km s^{-1})	EW^f (eV)	L^g ($\log[\text{ergs s}^{-1}]$)	C/bins
NGC 4051	0.002	RQ	1.513	0.013	h	6.420(6.391-6.447)	6160(3180-10870)	179(117-244)	41.176	284/283
NGC 4151	0.003	RQ	1.406	0.020	3.265	6.389(6.385-6.394)	2510(1970-3160)	83.1(75.9-94.7)	42.605	350/283
NGC 7314	0.005	RQ	1.517	0.014		6.412(6.399-6.423)	1000f	57.7(33.2-80.9)	42.256	317/283
NGC 5506	0.007	RQ	1.751	0.037	3.282	6.411(6.395-6.418)	3350(1240-4480)	90.5(72.0-116)	42.933	245/283
<i>MC G</i> – 6 – 30 – 15 ⁱ	0.008	RQ	6.408(6.349-6.454)	3250(0-12670)	49(12-101)	42.623	...
NGC 4593	0.009	RQ	1.689	0.023		6.403(6.390-6.410)	2200(0-5670)	72.6(48.1-100)	42.892	290/283
NGC 3783	0.009	RQ	1.668	0.083	0.874	6.398(6.387-6.410)	2420(840-4010)	92.1(64.4-118)	43.114	318/283
NGC 3516	0.009	RQ	0.866	0.029	1.171	6.398(6.383-6.417)	4320(3030-7020)	146(112-201)	42.574	301/283
MKN 766	0.012	RQ	1.950	0.017		6.421(6.393-6.457)	1000f	30.5(10.5-71.9)	42.855	264/283
IC 4329a	0.016	RQ	1.681	0.044	0.232	6.404(6.388-6.415)	1000f	25.8(12.1-36.1)	43.996	297/283
NGC 5548	0.017	RQ	1.589	0.017		6.399(6.386-6.414)	1690(0-2980)	66.5(48.7-90.9)	43.292	283/283
NGC 7469	0.017	RQ	1.804	0.049		6.391(6.376-6.401)	1100(0-4200)	91.3(61.0-127)	43.238	289/283
NGC 526a	0.019	RQ	1.081	0.022	0.046	6.405(6.383-6.423)	1000f	53.5(14.3-96.8)	43.355	317/283
ARK 564	0.025	RQ	2.388	0.063		6.4f	1000f	$\lesssim 56.5$	43.568	252/283
MKN 590	0.027	RQ	1.704	0.027	0.400	6.4f	1000f	121(69.6-186)	43.140	269/283
MKN 290	0.030	RQ	1.700	0.017	0.845	6.429(6.378-6.521)	3900(0-43540)	58.5(15.1-115)	43.513	242/283
MKN 279	0.031	RQ	1.616	0.018		6.423(6.393-6.458)	5240(3270-8130)	135(87-203)	43.472	322/283
MKN 509	0.035	RQ	1.621	0.041	0.016	6.426(6.403-6.448)	2860(0-6550)	47.4(25.6-75.2)	44.195	236/283
NGC 985	0.043	RQ	1.581	0.029	1.317	6.387(6.3728-6.410)	1000f	84.0(43.4-142)	43.656	298/283
ESO 198-G24	0.045	RQ	1.498	0.045		6.387(6.372-6.400)	1000f	94.1(49.6-142)	43.459	346/283
F9	0.046	RQ	1.688	0.033		6.409(6.385-6.432)	3780(2310-7240)	80.1(58.7-152)	44.039	256/283
MRC 2251-178	0.064	RQ	1.517	0.027	0.407	6.4f	1000f	22.5(7.76-38.9)	44.404	315/283
IRAS 13349+2438	0.107	RQ	2.298	0.012	2.306	6.417(6.365-6.438)	2940(230-8270)	58.5(36.6-147)	44.070	313/283
PDS 456	0.184	RQ	1.854	0.200	1.049	6.4f	1000f	$\lesssim 17.6$	44.544	373/283
H 1821+643	0.297	RQ	1.904	0.041	3.107	6.4f	1000f	40.1(17.6-64.1)	45.598	290/283
NGC 3227	0.003	RL	1.389	0.021	1.833	6.4f	1000f	$\lesssim 72.9$	41.670	318/283
MKN 421	0.031	RL	2.992	0.014		6.4f	1000f	$\lesssim 132$	44.034	350/283
3C 120	0.033	RL	1.636	0.111	0.055	6.418(6.404-6.428)	1410(0-3810)	57.2(34.8-85.8)	44.067	305/283
4C 74.26	0.104	RL	1.958	0.121	2.977	6.259(6.243-6.271)	1000f	40.4(17.6-65.8)	44.886	301/283
PKS 2155-304	0.116	RL	2.937	0.017	1.160	6.4f	1000f	$\lesssim 13.6$	45.168	277/283
H 1426+428	0.129	RL	2.226	0.032		6.4f	1000f	15.7(3.79-28.9)	45.241	265/283
3C 273	0.158	RL	1.796	0.018	0.261	6.4f	1000f	$\lesssim 6.69$	45.795	297/283
1 ES 1028+511	0.361	RL	2.574	0.012	2.340	6.366(6.310-6.381)	1000f	29.5(7.46-57.6)	45.770	275/283
3C 279	0.538	RL	1.740	0.022	2.097	6.564(6.548-6.584)	1000f	25.7(8.72-41.2)	46.248	285/283

Note. — Table 1 All parameters are quoted in the source rest frame. Statistical errors are for the 90% confidence level.

^aRedshifts obtained from *Quasars and Active Galactic Nuclei (11th Ed.)* (Veron+, 2003)

^bGalactic column density

^cintrinsic absorption

^dGaussian line center energy

^eFWHM, rounded to 10 km s^{-1}

^fEmission line equivalent width

^g2.–10. keV source frame luminosity

^hthe intrinsic absorption value $\lesssim 10^{-5}$ and we ignored intrinsic absorption in our model
ⁱthis fitting result was quoted from Yaqoob's Paper

Table 2. Parameters of the Narrow Fe K α Emission Line from *XMM-Newton*

Source	Redshift	Spectral Type	EW (eV)	Luminosity (log[ergs s ⁻¹])	Ref.
NGC 4151	0.003	RQ	187(184-190)	42.27	1
NGC 5506	0.006	RQ	70(50-90)	42.83	1
MCG-6-30-15	0.008	RQ	52(42-62)	42.90	1
NGC 3516	0.009	RQ	196(174-218)	42.39	1
NGC 4593	0.009	RQ	98(77-119)	43.07	1
Mrk 766	0.013	RQ	45(10-80)	43.16	1
IC 4329a	0.016	RQ	30(18-42)	44.77	1
Mrk 359	0.017	RQ	220(146-294)	42.49	1
Mrk 1044	0.017	RQ	186(125-247)	42.55	1
NGC 5548	0.017	RQ	59(53-65)	43.39	1
Mrk 335	0.026	RQ	$\lesssim 54$	43.27	1
Mrk 896	0.026	RQ	180(93-267)	42.70	1
Mrk 493	0.031	RQ	$\lesssim 101$	43.20	1
Mrk 509	0.034	RQ	85(28-142)	44.68	1
Mrk 841	0.036	RQ	$\lesssim 83$	43.89	1
1H 0707-495	0.041	RQ	$\lesssim 90$	42.23	1
ESO 198-G24	0.046	RQ	104(55-153)	43.27	1
Fairall 9	0.047	RQ	139(113-165)	43.97	1
Mrk 926	0.047	RQ	$\lesssim 61$	44.14	1
Ton S180	0.062	RQ	$\lesssim 64$	43.62	1
MR 2251-178	0.064	RQ	$\lesssim 74$	44.46	1
Mrk 304	0.066	RQ	$\lesssim 115$	43.82	1
Mrk 205	0.071	RQ	60(35-85)	43.95	1
HE 1029-1401	0.086	RQ	$\lesssim 105$	44.54	1
Mrk 1383	0.086	RQ	77(31-123)	44.10	1
1H 0419-577	0.104	RQ	$\lesssim 85$	44.56	1
Mrk 876	0.129	RQ	96(37-155)	44.19	1
Q 0056-363	0.162	RQ	$\lesssim 159$	44.23	1
PDS 456	0.184	RQ	$\lesssim 18$	44.77	1
Q 0144-3938	0.244	RQ	152(102-202)	44.34	1
UM 269	0.308	RQ	$\lesssim 99$	44.47	1
PB 05062	1.77	RQ	$\lesssim 61$	46.87	1
1 Zw 1	0.061	RQ	34(4-64)	43.85	2
Akn 564	0.025	RQ	$\lesssim 41$	43.50	2
NGC 4051	0.002	RQ	93(82-104)	41.39	2
NGC 7314	0.005	RQ	42(22-62)	42.28	2
Mrk 279	0.031	RQ	71(46-96)	43.50	2
NGC 3783	0.010	RQ	120(106-134)	43.03	2
NGC 7213	0.006	RQ	82(66-98)	42.27	2
NGC 7469	0.016	RQ	105(80-130)	43.17	2
SBS 0909+532	1.376	RQ	200(125-275)	44.71	4
PG 0157+001	0.163	RQ	$\lesssim 330$	43.85	3
PG 0804+761	0.100	RQ	100(40-170)	44.46	3
PG 0844+349	0.064	RQ	$\lesssim 100$	43.74	3
PG 0947+396	0.206	RQ	120(60-180)	44.35	3

Table 2—Continued

Source	Redshift	Spectral Type	EW (eV)	Luminosity (log[ergs s ⁻¹])	Ref.
PG 0953+414	0.234	RQ	$\lesssim 50$	44.73	3
PG 1048+342	0.167	RQ	100(40-160)	44.04	3
PG 1114+445	0.144	RQ	100(60-130)	44.16	3
PG 1115+080	1.722	RQ	$\lesssim 130$	45.81	3
PG 1115+407	0.154	RQ	$\gtrsim 100$	43.93	3
PG 1116+215	0.177	RQ	$\gtrsim 80$	44.49	3
PG 1202+281	0.165	RQ	$\gtrsim 80$	44.43	3
PG 1206+459	1.158	RQ	$\lesssim 350$	45.17	3
PG 1211+143	0.081	RQ	40(10-60)	43.70	3
PG 1216+069	0.331	RQ	$\gtrsim 70$	44.68	3
PG 1244+026	0.048	RQ	$\gtrsim 150$	43.15	3
PG 1307+085	0.155	RQ	$\gtrsim 110$	44.08	3
PG 1322+659	0.168	RQ	180(70-290)	44.03	3
PG 1352+183	0.152	RQ	150(70-230)	44.13	3
PG 1402+261	0.164	RQ	$\lesssim 100$	44.15	3
PG 1407+265	0.940	RQ	$\lesssim 30$	45.61	3
PG 1411+442	0.090	RQ	250(190-380)	43.40	3
PG 1415+451	0.114	RQ	110(30-190)	43.60	3
PG 1427+480	0.221	RQ	90(30-140)	44.20	3
PG 1440+356	0.079	RQ	$\lesssim 80$	43.76	3
PG 1444+407	0.267	RQ	$\gtrsim 180$	44.11	3
PG 1626+554	0.133	RQ	$\lesssim 160$	44.16	3
PG 1630+377	1.476	RQ	600(300-900)	45.32	3
PG 1634+706	1.334	RQ	$\lesssim 82$	46.11	3
NGC 3227	0.004	RL	191(168-214)	41.37	1
3c 120	0.033	RL	54(31-77)	43.97	2
PKS 1637-77	0.043	RL	$\lesssim 95$	43.73	1
3 Zw 2	0.089	RL	$\gtrsim 84$	44.34	1
PKS 0558-504	0.137	RL	$\gtrsim 11$	44.63	1
3C 273	0.158	RL	$\lesssim 9$	45.72	1
B2 1028+31	0.178	RL	88(43-129)	44.26	1
B2 1721+34	0.206	RL	63(29-97)	44.90	1
B2 1128+31	0.289	RL	50(11-89)	44.72	1
S5 0836+71	2.172	RL	16(10-22)	47.71	1
PKS 2149-30	2.345	RL	$\lesssim 40$	47.05	1
PKS 0438-43	2.852	RL	$\gtrsim 26$	46.93	1
PKS 0537-286	3.104	RL	$\lesssim 82$	47.46	1
PKS 2126-15	3.268	RL	$\lesssim 17$	47.48	1
S5 0014+81	3.366	RL	$\lesssim 17$	47.23	1
PG 0007+106	0.089	RL	$\gtrsim 60$	44.146	3
PG 1100+772	0.312	RL	60(20-100)	45.049	3
PG 1226+023	0.158	RL	$\lesssim 7$	45.708	3
PG 1309+355	0.184	RL	180(140-260)	43.826	3
PG 1512+370	0.371	RL	120(60-180)	44.946	3

Note. — The luminosities were calculated for the 2–10 keV rest frame.

References. — (1) Page et al. (2004a); (2) Zhou & Wang (2005); (3) Jiménez-Bailón et al. (2005); (4) Page et al. (2004b)

Table 3. Results of Linear Regression

Sample	Number of objects	Slope coefficient	Spearman’s coefficient
Chandra (RQ+RL)	34	-0.1940 ± 0.0332	-0.651
Chandra (RQ)	25	-0.1759 ± 0.0493	-0.520
XMM (RQ+RL)	89	-0.2097 ± 0.0503	-0.463
XMM (RQ)	69	-0.1023 ± 0.0558	-0.280
Combined (RQ+RL)	101	-0.2015 ± 0.0426	-0.469
Combined (RQ)	75	-0.1019 ± 0.0524	-0.266